(Received 14 December 2023, Accepted 21 January 2024, Scheduled 5 February 2024)

Information-Theoretic Measures for Reconfigurable Metasurface-Enabled Direct Digital Modulation Systems: An Electromagnetic Perspective

Xuyang Bai[1,2], Shurun Tan[1,2,3,*], Said Mikki[1,3], Erping Li[1,2], and Tie-Jun Cui[4]

[1] *Zhejiang University-University of Illinois at Urbana-Champaign Institute, Zhejiang University, Haining 314400, China*
[2] *State Key Laboratory of Modern Optical Instrumentation, College of Information Science and Electronic Engineering Zhejiang University, Hangzhou* 310027*, China*
[3] *Department of Electrical and Computer Engineering, University of Illinois at Urbana-Champaign, Urbana IL* 61801*, USA*
[4] *State Key Laboratory of Millimeter Waves, Southeast University, Nanjing* 210096*, China*

ABSTRACT: The fusion of electromagnetic (EM) waves and information theory in wireless and waveguide communication technologies has enjoyed a remarkable revival during the last few years. In particular, unlike traditional transceiver systems, the recently proposed information metasurface system directly links the controllable binary array sources with the scattered EM waves, making the combination of EM and information theories highly desirable and natural. Moreover, a traditional linear channel matrix cannot be directly used for such scattering reconfigurability enabled communication system, making the information characterization of such system a great challenge. In this paper, EM information characteristics of a direct digital modulation (DDM) system enabled by programmable information metasurface, also known as reconfigurable intelligent surface (RIS), are analyzed, in which RIS is used as a modulator of the illuminating field, while the scattered far-field amplitudes are measured and effectively treated as the received quantities. The posterior probability for a specific source coding pattern, conditioned over a given measured scattering fields, is obtained through the Bayesian analysis technique, from which the average mutual information (AMI) is obtained to estimate the RIS observation capability along any particular direction. The averaged receiver mutual information (ARMI) is then introduced to characterize the generated field correlation structures along different observation directions. Based on ARMI, the joint observation capability is also analyzed. Furthermore, the suggested techniques are employed in a noisy environment, and a code selection scheme is put forth to achieve efficient information transmission. The proposed configuration is validated through a simulated experiment. As a comprehensive evaluation of the system's performance, the channel capacity of the system is derived, and a set of relevant influencing factors are identified and analyzed from four different perspectives: 1) the observation direction, 2) the size of RIS, 3) potential joint observations in multiple directions, and 4) the noise level. The proposed method, together with the various related performance measure metrics introduced therein, are expected to provide the research community with guidelines for analyzing and designing the current and future RIS-based communication systems, which can also be extended to other aspects in the growing field of the EM information theory.

1. INTRODUCTION

In wireless communication scenarios, accurate modeling of the transmission channel characteristics from a full-wave electromagnetic (EM) analysis can be difficult due to complex propagation environments and the coupling of propagating waves in space and time [1]. As a result, in the field of communication theory, the focus is typically on the temporal aspects of the carrier, while the spatial characteristics of the EM waves are often simplified as in multipath fading models [2]. In recent years, with emergent new application scenarios such as near-field communication [3, 4], indoor communication [5], and dense antenna communication [6], the necessity to model and analyze the spatial characteristics of waves in various communication systems is growing [7, 8]. The introduction of an electromagnetic theory of information, where the electromagnetic scattering physics is seamlessly connected to and incorporated into the information theory, would help overcoming some of the shortcomings arising from the absence of a detailed and comprehensive understanding of spatial correlations in statistical models of modern wireless technology [9], hence allowing the spatio-temporal characteristics of information to be effectively expressed and exploited in order to improve the performance of various data transmission and processing systems [9–14].

In traditional wireless communication systems, information is first converted to a digital baseband signal, and then passed through a digital modulation process in order to improve the noise immunity of the system [2], before it is injected into the radio-frequency carrier signal, often resulting (when properly designed) in high-data rate links [15]. In such systems, information is confined to carrier characteristics such as the amplitude, phase and frequency. The EM information analysis deployed in traditional communication system theory starts from

* Corresponding author: Shurun Tan (srtan@intl.zju.edu.cn).

an accurate model of the antenna radiation fields, especially the near fields [16–19]. Subsequently, the channel matrix H is obtained from the deterministic fields, then linked into some basic metrics taken from information theory in order to analyze important aspects in the EM communication system such as the channel capacity [12, 16, 20], channel degree of freedom [21, 22], antenna element layout and array design [23], in addition to the relevant power allocation considerations and efficient on-site EM correlation estimation as manifested in various possible practical scenarios [24]. In the last few years, Reconfigurable Intelligent Surfaces (RISs) have also been a prime catalyst pushing toward a better understanding of how information and physical aspects of the communication environment relate to each other [25–28]. Since these structures are intended to modify the channel transmission characteristics in ways conductive to improving spectral efficiency, latency, and power constraints, they provide an excellent opportunity to link the physical degrees of freedom with the purely signal processing aspects of the communication system [28–30]. Here, it appears that the main contribution is the enormous usefulness of the idea of *reconfigurablity* and electronic adaptability of a given system to the environment and vice versa [25, 26, 31, 32].

In recent years, the introduction of various strategies for performing digital coding using information metasurfaces [33, 34] has required researchers to directly combine information data transmission with a more detailed knowledge of the fine details of EM scattering by complex structures, making it inevitable to apply the crossdisciplinary field of EM information theory to the full analysis of such complex and not yet fully understood systems. Additionally, research has shown that one-bit coding of RIS can yield satisfactory performance in most practical scenarios [35]. It demonstrates the capabilities of digital coding RISs in electromagnetic information systems and underscores the significance of further research to fully characterize such EM information systems. Cui et al. first proposed a direct digital modulation (DDM) system based on the RIS [36], in which the coding metasurface is directly controlled by the source digits through a field programmable gate array (FPGA), and the far-field is directly measured by the receiver to decode the information and realize communications. In such a DDM system, which is distinct from the conventional communication systems, information is directly modulated by the metasurface itself while operating in the scattering mode. On the other hand, the decoding process at the receiver side is strictly constrained by the locations of the receivers, demonstrating clear advantages in terms of simplicity, design, and security. Subsequently, inspired by the time-division multiplexing schema in digital communications, frequency-division multiplexing, and other multiplexing techniques in information systems [2], metasurface systems for temporal-spatial modulations were recently proposed [37], and different modulation methods have also been explored for DDM application scenarios, including, for example, amplitude shift keying (ASK), frequency shift keying (FSK) [38], phase shift keying (PSK) [39], and quadrature amplitude modulation (QAM) [40, 41]. Overall, currently existing researches on such information metasurface have enabled the development of communication systems exploiting unique designs and special settings based on EM reconfigutablity [42, 43].

Nevertheless, in spite of the progress already made in terms of design, testing, and implementation, a comprehensive and detailed systematic theoretical analysis of the performance of such systems with respect to various system parameters has not received the attention it deserves. In a previous work, Cui et al. proposed the concept of metasurface information entropy in order to evaluate the information carrying capabilities of metasurfaces, including information transfer in space-time domains [44–47]. However, to the best of our knowledge, a detailed transmission mechanism of the reconfigurable cells' digital data from source to destination or observation locations has not been considered before. There also exists a parallel research direction that substitutes multiple-input-multiple-output (MIMO) [48] system's antennas with metasurfaces, after which one proceeds to analyze the obtained metasurface-based system's performance using the information theory of MIMO systems [49, 50]. However, it is noteworthy that such a DDM system is fundamentally different from a MIMO system in terms of information characterization. In a conventional information system, one can adopt the well understood linear channel model $\mathbf{y} = \mathbf{H}\mathbf{x}(\mathbf{s}) + \mathbf{n}$ [49] to represent the channel by its channel matrix $\mathbf{H}$, where the transmitted signal $\mathbf{x}$ is connected to the information source $\mathbf{s}$ through a mapping $\mathbf{x}(\mathbf{s})$. In such analysis, the channel matrix $\mathbf{H}$ linking the transmitted signal $\mathbf{x}$ to the received signal $\mathbf{y}$ is independent of the information source $\mathbf{s}$, though $\mathbf{H}$ could vary with time or adjust to transmitter/receiver locations as in the RIS aided MIMO systems. However, for the RIS-DDM system discussed in this paper, the variations in the scatterers, i.e., different states of the RISs, directly carry information. The mathematical model can be abstracted as $\mathbf{y} = \mathbf{H}(\mathbf{s})\mathbf{x} + \mathbf{n}$, where the source information $\mathbf{s}$ is being delivered through modulating the properties of the channel $\mathbf{H}$, i.e., the scattering characteristics of the metasurface, while the transmitted signal $\mathbf{x}$ (the illuminating field from the transmitting antenna) is irrelevant to the information being carried. An equivalent representation [47] would be again to represent the system with $\mathbf{y} = \mathbf{H}\mathbf{x}(\mathbf{s}) + \mathbf{n}$ where a stationary $\mathbf{H}$ is extracted (related to the free space wave propagator or the Green's function in the field analysis language) while our concern is to link $\mathbf{s}$ directly to $\mathbf{y}$ rather than connecting $\mathbf{x}$ (corresponding to the equivalent current J induced on the metasurfaces) to $\mathbf{y}$ as in the traditional theory. All these interpretations deserve new development in theoretical characterization as discussed in this paper.

Overall, the authors believe that a systematic and computationally-efficient framework combining electromagnetic and information theories for the purpose of analyzing RIS-DDM systems is still missing, and it would be highly desirable to propose one. The present article's main objective is attempting to introduce a contribution toward filling this gap by defining several useful and implementable EM information performance measures aiming at describing the information content of such systems, as well as to analyze the impact of several external configurations influencing the information-handling capacity of such systems. The proposed performance measures introduced below include:

1. The average mutual information (AMI), whose aim is to describe the information-theoretic observation capability of the digital-modulated metasurface as effected along any given particular direction.
2. The averaged receiver mutual information (ARMI) and the joint average mutual information (JAMI), which, respectively, are used in order to characterize the correlation of the scattered electromagnetic fields along multiple observation directions and to estimate the joint information transmission capacity with multiple observations taken simultaneously.
3. The Shannon information channel capacity, which is needed in order to estimate the theoretical upper bound on the maximal information data transmission capability.

On the other hand, influencing factors taken into consideration below include the receiver direction, the size of the information metasurface, potential joint observations in multiple directions, and the noise level. Our overall methodology is based on the joint utilization of the principles of electromagnetic theory and Shannon information theory [51], which provides a more accurate evaluation for the quantitative characterization of the system performance, while it may help guide the development of both current and future advanced telecommunication systems that exploit the advantage of deeper understanding of electromagnetics in the information transmission system design itself.

2. THE DDM SYSTEM AND FAR-FIELD STATISTICS

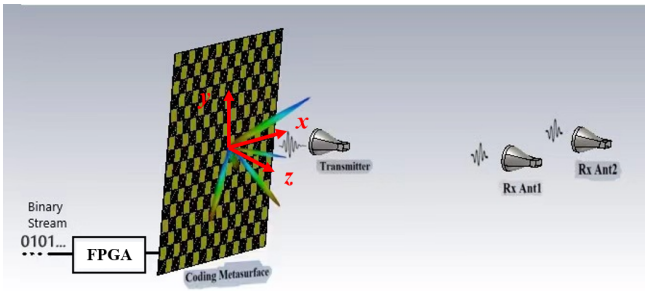

FIGURE 1. An illustration to the RIS-enabled DDM system.

The goal of the RIS-enabled DDM system (Fig. 1) is to externally modify the scattered EM field fingerprints that correspond to each coding pattern supplied to the programmable metasurface. This modification enables the system to manipulate, store, and transmit information. The system decodes the scattered far fields detected by the receivers into the coding pattern of the metasurface. The coding pattern is controlled by the digital source, which utilizes FPGAs on the metasurface substrate. Unlike most current wireless communication technologies, DDM systems do not use amplitude, frequency, or phase modulation of the carrier wave to transmit the digital baseband signals carrying information. Instead, they utilize the far-field scattering pattern in modulation, where the digital baseband signals directly affect various far-field scattering distributions of the electrical signal.

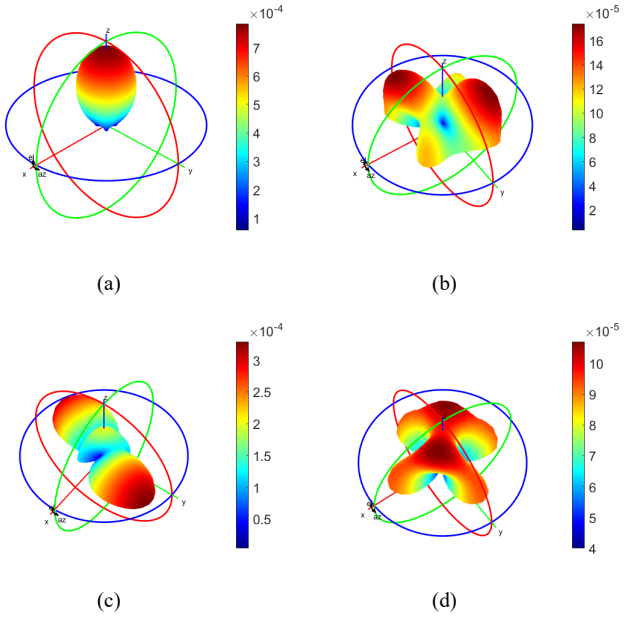

FIGURE 2. Exampled far field patterns for modulation in the DDM system. (a) S_A corresponds to 00. (b) S_B corresponds to 01. (c) S_C corresponds to 10. (d) S_D corresponds to 11.

To demonstrate the far-field modulation mode and practical implementation of the DDM system, a compelling example is provided. Fig. 2 shows four different metasurface scattering patterns named S_A, S_B, S_C and S_D, which are used as the modulation of the baseband codes 00, 01, 10, and 11, respectively. The encoding sequence of the RISs (defined as the RIS hardware code) associated with these scattering patterns are 1, 3855, 9925, and 42405, respectively, for the 4×4 RIS considered in this study, corresponding to the RIS binary sequences of 0000000000000000, 0000111100001111, 0010011011000100, and 1010010110100101, respectively. The detailed mapping between the metasurface patterns and the RIS binary sequence (or defined hardware codes) is explained as follows in this section. Consider a digital information flow to be transmitted, "1010001101," which can be broken down into "10 10 00 11 01." By manipulating the information metasurface, a far-field distribution of "S_C-S_C-S_A-S_D-S_B" can be generated in a time sequence, and the information flow can be demodulated from the observation of the far-field (provided the correspondence between the far-field and baseband code is clear at the receiver). However, in practice, it is challenging to observe the total scattering pattern in all directions. It is therefore more efficient to establish a correlation between the far-field observations in a single direction or a limited number of directions with the baseband codes. This is what is referred to as single direction observation and multi-direction joint observation in this paper. In traditional amplitude or phase modulation, the modulation signal is designed first, and then a circuit is designed to produce the desired modulation wave. However, in DDM systems, the far-field scattering patterns are limited by the size and reconfigurability of the metasurface, and cannot be randomly devised. A crucial aspect of DDM systems is determining the number of possible far-field patterns and what metasurface pattern regulations should be applied to obtain those scattering patterns.

This process heavily relies on the observation directions, noise levels, and single or joint observations.

It is important to note that even though the far-field pattern is used as the modulation mode, the specific metasurface pattern controlled by the metasurface code (hardware code) remains the source of the system, with the scattering far-field to be observed by the receiver. As a result, the DDM system has the potential to provide enhanced security, optimized utilization of the spatial characteristics of the wave, and a more streamlined configuration than traditional amplitude modulation systems [36]. Moreover, the DDM concept may be combined with the traditional RIS-MIMO mechanism, offering a new dimension of freedom to carry information by the RIS patterning. Fig. 3 displays a flowchart that visually represents the information transmission process of the DDM system. It demonstrates how the system relies on far-field directions, its multi-directional observation capability, and its lack of complex modulation circuits.

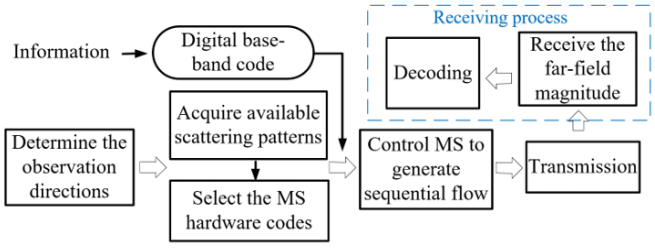

FIGURE 3. Information transfer flow chat for RIS (MS) based DDM system.

In the computational examples that follow, we utilize 3×3 and 4×4 coding metasurface configurations operating under normal illumination conditions. In practical applications, to justify the periodic boundary condition in modeling the metasurface scattering phases, each metasurface elements are usually repeated several times to form a larger surface while maintaining limited degrees of freedom. For instance, a 20×20 metasurface can be utilized, but every 5×5 cells are tied to the same control signal, making the system degree of freedom essentially 4×4. While a 20×20 metasurface with completely independent units would offer a greater degree of freedom in theory, it would require significant computing resources to determine the receiving set of the system. Once the set of received values is determined, all the parameters, relations, and calculation methods proposed in this article remain fully effective and applicable. Therefore, the various investigative scenarios given below are chosen for simplicity without sacrificing generalizability. We also assume one or more power detection schemes at the receiver side. The metasurface is placed in the XOY plane with the center of the metasurface at the origin O. We assume that each cell of the metasurface can vary independently of the states of other cells. Externally-controlled cell-by-cell binary information patterns can be practically realized by switching ON and OFF a grid of independently-controlled varactors, where each varacator is connected to a metasurface element [33]. The state of the varacator diode is controlled by a digital source: 1 and 0 correspond to the opening and closing of the diode, respectively, thus realizing the modulation of the information on the metasurface pattern. Therefore, a 4×4 metasurface supports 2^{16} different coding patterns (hardware codes), and a 3×3 metasurface supports 2^9 patterns.

In order to describe as clearly as possible the manner of how each hardware code and its associated binary pattern are dealt with in this paper, we refer to the decimal number of code as its hardware code number. To explain our method, we provide a simple but illustrative example. The 4×4 metasurface has a total of 2^{16} different kinds of hardware codes which are labeled in this paper as the 1st code, the 2ed code, the 3rd code, etc, up to the final label, the 2^{16}th code. The i-th code corresponds to the standard binary representation of $i-1$, and we name it RIS hardware code i. For example, the 9925th code, or RIS hardware code 9925, corresponds to 0010011011000100, where two zeros were prefixed in order to make the code fits into a 4×4 metasurface. In Fig. 4, we illustrate how this binary code schema of the 9925th code is assigned in an example of a 4×4 reconfigurable grid. The code is arranged on the metasurface following the order from top to bottom and from left to right as stated in the figure.

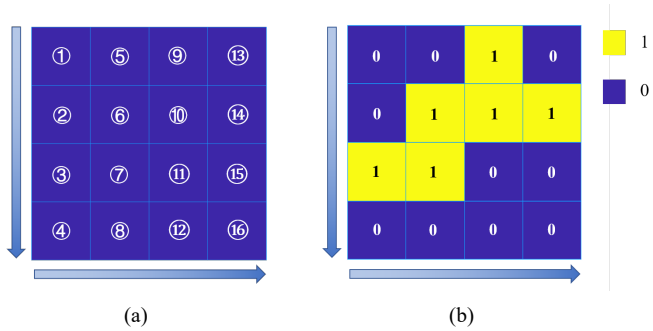

FIGURE 4. (a) The standard assignment pattern for a metasurface starts with cell 1 in the top-left corner and then fills the column downwards. The numbers 1, 2, etc., indicate the physical metasurface cell locations in the binary representation of the hardware code. Once a column is complete, the assignment moves to the next column to the right and starts again from the top with cell 5. This process repeats until the entire DDM grid is filled. By following this pattern, the hardware code can be accurately mapped to the precise distribution of ON and OFF states for all radiating cells. (b) An illustration of a metasurface pattern for an example code 9925.

2.1. Electromagnetic Far-Field Calculations

For modeling the scattering far fields, full-wave simulations are sometimes used due to their high accuracy [52–55]. However, a complete electromagnetic simulation of generic metasurfaces for stochastic analysis is currently unfeasible. More commonly, to speed up the calculation, accurate physics-based deterministic simulations are only applied for the reflection coefficients or surface equivalent currents of the cell unit, where it can be later combined with a physical optics (PO) approximation [56] in order to model the total far fields [57, 58]. In this paper, a Fourier transform (FT) approach, which is based on the PO framework, is adopted for the purpose of efficiently approximating the scattering far fields, the effectiveness of which has been validated in [44]. For simplicity, the equivalent current density of one

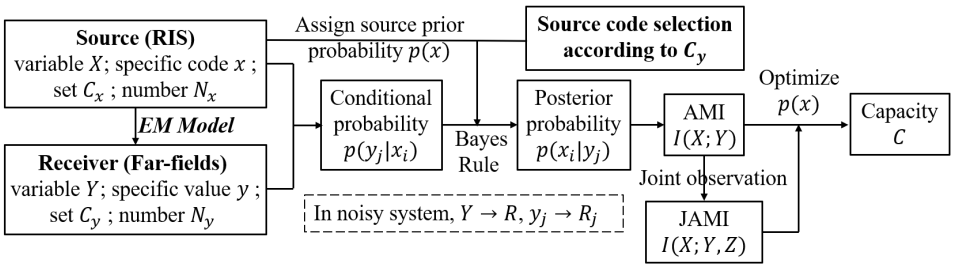

FIGURE 5. An illustration of the utilized symbols, and the interconnection and progression of diverse system parameters.

particle (unit cell) is taken as

$$J(x,y) = \begin{cases} J_0 e^{i\phi_0} & \text{for coding '0',} \\ J_0 e^{i(\phi_0+\pi)} & \text{for coding '1'.} \end{cases} \quad (1)$$

Note that, in general, Eq. (1) can take on arbitrary forms when describing the current distribution on metasurface elements. For instance, the amplitude of different states may vary. Nevertheless, these variations do not affect the proposed analyzing methodology but might introduce further computational complexity to characterize the current distribution. On the other hand, the far field can be derived from the FT of the equivalent current (1) as represented by the coding pattern. The scattering far field is given by, following [44]

$$E^s(r,\theta,\phi) = \frac{i\omega\mu_0}{4\pi r} e^{ikr} P(k\sin\theta\cos\phi, k\sin\theta\sin\phi), \quad (2)$$

where k is the wave number, while r, θ, ϕ are the spherical coordinates. The function P is the FT of the coding pattern, which has the form [44]

$$P(k\sin\theta\cos\phi, k\sin\theta\sin\phi) = \int_{-\frac{L_x}{2}}^{\frac{L_x}{2}} \int_{-\frac{L_y}{2}}^{\frac{L_y}{2}} \mathrm{d}x'\mathrm{d}y' J(x',y') e^{-i\left(kx'\sin\theta\cos\phi + ky'\sin\theta\sin\phi\right)}. \quad (3)$$

Formula (2) shows that distance r only affects the far-field pattern through an additional coefficient, not its distribution. Hence, the analysis will focus on a single distance, and calibration of the coefficient is needed for other distances. We choose far-field locations satisfying $r = \omega\mu_0/(4\pi)$ for the receiver, while we use the magnitude of the scattering far-field $|E^s|$ as the observation values. The frequency of the illuminating wave is 10 GHz, and the metasurface element size is 7 mm. As a result of the above approximation, the far-field distribution for any coding pattern can be efficiently and directly calculated in any specified direction. As examples, Fig. 2 illustrates the simulated distributions of scattering far-field $|E^s|$ for four different metasurface hardware code, 1, 3855, 9925, and 42405.

To clearly illustrate our analysis approach for this novel RIS-DDM system, the various symbols utilized, as well as the interconnection and progression of diverse system parameters to be discussed, are summarized in Fig. 5. We begin by identifying the discrete states of the source (RISs) and subsequently apply the EM model to determine the discrete states of the receiver. This establishes the connection between source and receiver, forming the core of the EM information strategy discussed in this article. Subsequently, we can determine the conditional probability for each possible source-receiver combination. Based on a specific prior probability assumption, the posterior probabilities of each source-receiver combination can be next obtained, and the average mutual information of the system can be calculated to evaluate the performance of the system under a specific encoding state. And the channel capacity of the system can be obtained by optimizing the prior probability, providing an assessment of the overall system performance.

2.2. Source Entropy, Receiving Value, and Posterior Probability

2.2.1. Source Entropy

Following Shannon information theory, the source, i.e., the RIS hardware codes, modeled as a random variable X, has an entropy defined as [51],

$$H(X) = -\sum_{i=1}^{N_x} p(x_i)\log_2 p(x_i), \quad (4)$$

where x_i represents the ith source hardware code (the RIS hardware code i). Recall that the source x we considered in this paper is directly linked to the information **s**, rather than serving as a carrier signal. $p(x_i)$ is its prior probability, while N_x is the number of all the possible RIS patterns, i.e., the number of source. For example, in the case of an 4×4 information metasurface, distribution of all hardware codes with a total number of $N_x = 2^{16}$, corresponds to a source entropy of 16 bits when they are all assigned a equal prior probability.

In the following, we may firstly deduce from single-direction observations in zero channel noise scenarios. The concepts for multi-observation cases are similar, with only a difference in the form of the received value, which will be discussed in Section 4.

2.2.2. Receiving Value and Its Set

In the absence of channel noise (noisy scenarios will be considered in Subsection 3.3), a specific source random variable $X = x$ (the RIS hardware code) will have a uniquely determined scattered far field $Y = y$ (Y is the receiving random

variable, and y is one of its specific value), with a generic functional form $y = f(x)$, where f is the input-output relation. This relation is ultimately based on the physical (Maxwell's) theory of electromagnetic scattering, here approximated by the PO formula (2) above[1]. Therefore, a distinct variable $y(\theta, \phi, x_i) \in C_y(\theta, \phi)$ may be assigned to represent the received far-field value in direction (θ, ϕ) for a specific source x_i, where the set of all possible observation values in a given direction is denoted by $C_y(\theta, \phi)$. The set $C_y(\theta, \phi)$ can be obtained by traversing all RIS hardware codes (from $i = 1$ to $i = 2^{16}$ for the 4×4 metasurface, as shown on the horizontal axis of Fig. 6). The receiving value $y(\theta, \phi, x_i)$ is a discrete variable, and its value set $C_y(\theta, \phi)$ is finite. The number of values that can be taken by y, i.e., the size of $C_y(\theta, \phi)$, is denoted by $N_y(\theta, \phi)$. Recall that N_y can be readily obtained from traversing all the RIS hardware codes and counting from all the obtained receiving values.

Note that, since multiple metasurface coding patterns, i.e., the RIS hardware codes, may correspond to the same far-field observation value at a given direction considering the symmetry, the number of receiving values N_y will be smaller than the number of source N_x. Table 1 shows the total source pattern number N_x under three different metasurface sizes and the number of observation value N_y in three different observation directions. Obviously, N_y is much smaller than N_x.

TABLE 1. Source number and receiver value number for different size metasurface DDM systems.

RIS size	N_x	Maximum source entropy	Observe direction	N_y
2×2	16	4 bit	$\theta = 45°$, $\phi = 0°$	5
			$\theta = 13.5°$, $\phi = 36°$	8
			$\theta = 54°$, $\phi = 72°$	8
3×3	512	9 bit	$\theta = 45°$, $\phi = 0°$	19
			$\theta = 13.5°$, $\phi = 36°$	116
			$\theta = 54°$ $\phi = 72°$	134
4×4	65536	16 bit	$\theta = 45°$, $\phi = 0°$	120
			$\theta = 13.5°$, $\phi = 36°$	535
			$\theta = 54°$, $\phi = 72°$	476

As a specific example to illustrate our strategy to obtain $C_y(\theta, \phi)$, and to clearly show the relation of its size $N_y(\theta, \phi)$ with the source number N_x, in Fig. 6, observation values represented by the far electric field magnitude conducted at $\theta = 45°$, $\phi = 0°$, cf. Fig. 6(a), and $\theta = 13.5°$, $\phi = 36°$, cf. Fig. 6(b), for a 4×4 metasurface system under all the source hardware code numbers from 1 to 2^{16} are displayed. It can be seen that the observation values are discrete, while the relation is many-to-one (many hardware codes to the same $|E_s|$) due to symmetry. All the possible receiving values y shown in the vertical axis are combined to construct C_y, and the number of the values (the size of C_y) can be readily counted as N_y. Note that the number of distinct observation values in Fig. 6(b) is larger than

[1]Note that this relation does not adhere to a mere linear correlation; hence, in the DDM system, the receiving variable cannot be simplistically characterized as $y(x_i) = Hx_i$.

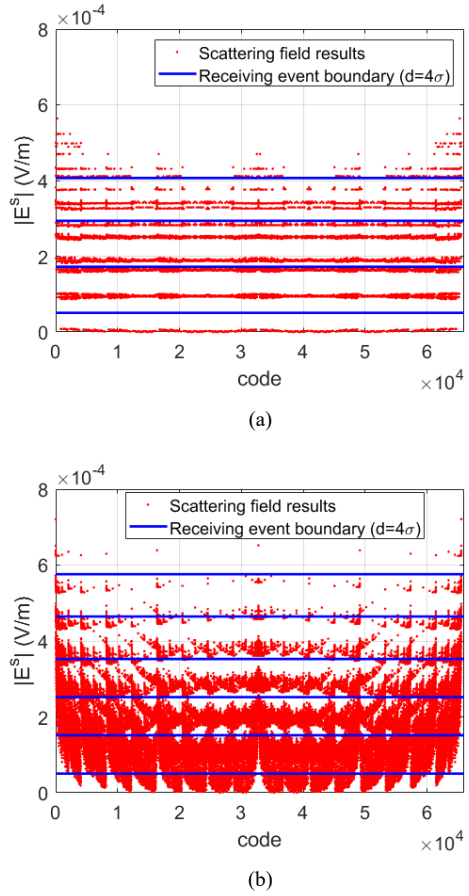

FIGURE 6. Observation values for each coding pattern with no channel noise. The horizontal axis is the decimal value corresponding to each code. (a) Observe in $\theta = 45°$, $\phi = 0°$. (b) Observe in $\theta = 13.5°$, $\phi = 36°$.

that in Fig. 6(a), indicating a better communication potential in the latter case, an observation that will be corroborated using information-theoretic measures to be introduced below.

2.2.3. Posterior Probability

As discussed in Section 2.2.2, based on the EM model and the traversal process, we can determine the complete range of receiving values, i.e., each individual element in C_y[2]. In order to facilitate our discussion, we organize them in ascending order and denote them as y_j ($j = 1, \ldots, N_y$, is ranked by the value in C_y from small to large). From this and due to the unique relation from a specific x_i to its scattered far-field, we deduce, in the noiseless RIS-DDM system,

$$p(y_j|x_i) = \begin{cases} 1, & \text{for } y_j = f(x_i), \\ 0, & \text{for } y_j \neq f(x_i). \end{cases} \tag{5}$$

[2]It is worth mentioning that expanding the digital RIS to a continuous RIS would result in the source x and receiver value y no longer being discrete. In this case, by leveraging beam-forming theory, we can determine a maximum value of y in the observation direction. From a certain segmentation, a finite number of y states can be readily obtained, ensuring the applicability of the proposed strategy in this article. It is also worthwhile to investigate a pure continuous system analysis methods under such a system. In this article, our focus is primarily on the digital RIS, which has limited states. Therefore, the acquisition of C_y can be achieved through a traversal process.

The posterior probability $p(x_i|y_j)$ can be readily estimated following the Bayesian rule [59]:

$$p(x_i|y_j) = \frac{p(x_i)p(y_j|x_i)}{\sum_{m=1}^{N_x} p(x_m)p(y_j|x_m)}, \quad (6)$$

where the sum in the denominator is performed over the set of all possible hardware codes of the DDM cell grid. Recall that the observation value y_j cannot be taken arbitrarily. Its possible values are calculated using the EM model, c.f. Eqs. (2), (3), and from the traversal of all the metasurface hardware codes.

It is natural then to define the set of source codes with the same observation value y_j as,

$$A_x(y_j) := \{x_m |\ y_j = f(x_m), m = 1, 2, 3, \ldots, 2^{N_x}\}. \quad (7)$$

Therefore, in the special case of equi-probably distributed sources, the posterior probability can be simplified as,

$$p(x_i|y_j) = \frac{p(y_j|x_i)}{\sum_m p(y_j|x_m)} = \begin{cases} \frac{1}{N[A_x(y_j)]}, & y_j = f(x_i), \\ 0, & y_j \neq f(x_i). \end{cases} \quad (8)$$

where $N[\cdot]$ is the cardinality (number of elements) of the set.

3. AVERAGE MUTUAL INFORMATION AND INFORMATION TRANSMISSION WITH A SINGLE OBSERVATION

3.1. Average Mutual Information

By employing Eqs. (5) and (6), we obtain the corresponding posterior probability associated with each source and receiving value, under a specific source prior probability distribution. Following the Shannon information theory, the conditional entropy $H(X|Y)$ can be subsequently calculated from [51],

$$H(X|Y) = \sum_{j=1}^{N_y} \sum_{i=1}^{N_x} p(y_j)\, p(x_i|y_j) \log_2 \frac{1}{p(x_i|y_j)}. \quad (9)$$

The quantity $H(X|Y)$ is the loss entropy, which represents the average uncertainty of the source random variable X given the observation Y.

Next, the average mutual information (AMI), denoted by $I(X;Y)$, is defined as the difference between the source entropy $H(X)$ and the conditional entropy $H(X|Y)$, giving rise to:

$$I(X;Y) = \sum_{j=1}^{N_y} \sum_{i=1}^{N_x} p(x_i)\, p(y_j|x_i) \log_2 \frac{p(x_i|y_j)}{p(x_i)}. \quad (10)$$

This quantity has a symmetry relation,

$$I(X;Y) = H(X) - H(X|Y) = H(Y) - H(Y|X) = I(Y;X). \quad (11)$$

This means that the evaluation of information flow in one direction is sufficient for determining the flow mechanism in the reverse direction.

In the original formulation by Shannon [51], the AMI is used to describe the average uncertainty in a system, i.e., the amount of information transmitted between the source and the receiver at a specific direction at an observation site that remains after the irreversible destruction of some of the original source's information due to uncertainty, mainly caused by noise in typical communication systems. In error-free communication, the receiver can eliminate all uncertainties of the source by observations, resulting in the AMI being identical to the source entropy.

Figure 7 depicts the distribution of AMI for the noiseless 4×4 metasurface system with respect to the observation directions under equi-probability sources. It is important to note that in a noiseless system, the received signals y_j of the DDM system are uniquely determined for a specific source coding pattern, resulting in complete determinism. Therefore, in this case, $H(Y|X) = 0$, and the AMI reduces to exactly the entropy of the observation value, $H(Y)$. The results presented in Fig. 7 show relatively high AMI values along the four main lobes. However, these values are less than the source entropy $H(X) = 16$ bit, indicating an ineffective communication configuration with potential decoding errors.

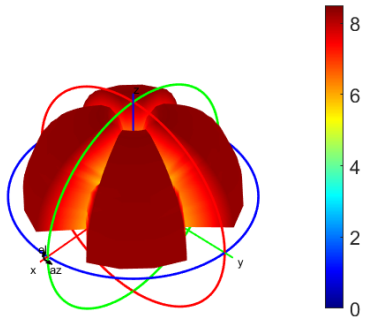

FIGURE 7. AMI angular distribution for equi-probability source coding 4×4 metasurface DDM system.

3.2. Information Transmission through Noiseless DDM Systems

To construct an effective information transmission system, we select only one code from those with the same scattering far-field value y_i to form a source coding set. The probabilities of other codes are set to zero, allowing us to construct a viable one-to-one correspondence mechanism. With this new configuration, the source X and receiver random variables Y have the same number of codes, and $p(y_i)$ is the same as $p(x_i)$. Therefore, we have,

$$I(X;Y) = H(Y) = H(X), \quad (12)$$

which is equivalent to an error-free communication scenario. Let us take the 4×4 metasurface DDM system as an example and set the observation direction along $\theta = 45°$, $\phi = 0°$. From the far-field results, we count $N_y = 120$ different y values. Codes with the same observation values are indistinguishable. Therefore, we are free to choose any hardware code from the set $A_x(y_j)$ corresponding to a given measured far-field value y_j. We choose the hardware code with the smallest code number in each group $A_x(y_j)$ and use it to carry information. Fig. 8(a) shows the selected hardware code numbers and the related scat-

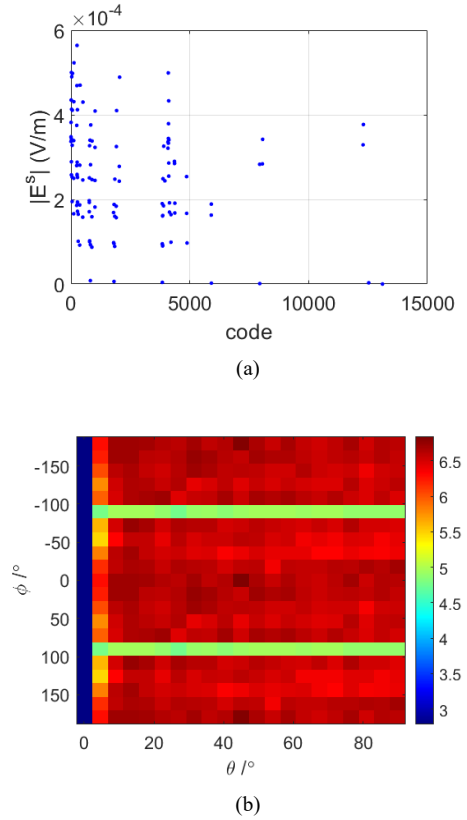

FIGURE 8. (a) Source coding and the related far field magnitude for an effective communication system. (b) AMI in different observation directions.

tering field magnitudes (recall that distinct values of y belonging to the same random variable Y at one far-field direction are indexed by $j = 1, \ldots, N_y$). Each selected code is assigned an equal probability distribution.The source entropy in this case is evaluated using Eq. (4) as 6.91 bit, same as the AMI in the chosen observation direction. This illustrates the fundamental information-theoretic measures in a basic digital communication system based on scattering information metasurfaces. The work in [36] provides an experimental realization of such systems.

Measures such as AMI may be utilized to assess the effectiveness of specific communication strategies against observation directions. Moreover, it can also provide information on the quality of detection at other directions. For the 6.91 bit source coding system for measuring at $\theta = 45°$, $\phi = 0°$, the AMI in different observation directions is calculated and shown in Fig. 8(b). It is noted that AMI reaches the maximum value of the source entropy only at $\theta = 45°$, $\phi = 0°$. At other locations, AMI is smaller than $H(X)$, hence degrading the quality of decision at the receiver side. This results from the fact that the chosen source codes for carrying information in the DDM system lead to mutually different far-field values only along the direction $\theta = 45°$, $\phi = 0°$, and the direction $\theta = 45°$, $\phi = 180°$ due to symmetry considering the normal incidence configuration, yet along other far-field directions some of these transmitting configurations yield identical far-field values. Meanwhile, relatively lower AMIs can be observed at directions $\phi = 90°$ and $\phi = -90°$ in ϕ directions orthogonal to the optimized direction of interest, again due to symmetry relations.

3.3. Information Transmission through a Noisy DDM Channel

As discussed in Section 2.2, for the noiseless system analyzed above, the conditional probability $p(y_j|x_i)$ is 1 when y_j matches the scattering field value under source code x_i, while for all other values of y_j, the conditional probability is 0. But for a communication channel with noise, a non-zero probability is linked to receiving other values. To maintain the discrete random variable math structure that we developed in earlier sessions, we discretize the receiver end and define an event R_j for the observation y_j falling within a range $y_L \leq y_j < y_H$ as follows

$$R_j = \{y_L \leq y_j < y_H\}, \tag{13}$$

where y_H and y_L are the decision bounds to be determined. The decision bounds are related to the adopted communication schemes. A maximum likelihood (ML) estimation for event R_j yields (please refer to the appendix for proof),

$$y_H = \frac{y_{j+1} + y_j}{2}, \quad y_L = \frac{y_{j-1} + y_j}{2}, \tag{14}$$

with $y_j, j = 1, \ldots, N_y$, ordered in an increasing order as discussed in Section 2.2. The y_L corresponding to R_1 is taken as 0, and the y_H corresponding to R_{N_y} is taken as infinite. The noise properties are yet to be carefully examined. In a first attempt, we assume an additive Gaussian noise with variance σ^2 and ignore potential channel fading effects. Then the conditional probability $p(R_j|x_i)$ is expressed as

$$p(R_j|x_i) = \int_{y_L}^{y_H} \frac{1}{\sqrt{2\pi}\sigma} e^{-\frac{1}{2}\left(\frac{y - y(x_i)}{\sigma}\right)^2} \mathrm{d}y, \tag{15}$$

where $y(x_i) = f(x_i)$ is the ideal observation value corresponding to the chosen source x_i. The standard deviation σ measures the noise level as linked to the signal-to-noise ratio (SNR). The variance σ^2 relates to the product of the receiver bandwidth and the noise power spectral density. For specifying the SNR level, the average value of the estimated scattering field random variable Y at the receiver under each selected code in the noise-free case is taken as the signal strength.

In lieu of Eq. (10), the AMI corresponding to the decision rule as specified by R_j is calculated by replacing y_j with the event R_j,

$$I(X;R) = \sum_{j=1}^{N_R} \sum_{i=1}^{N_x} p(x_i)\, p(R_j|x_i) \log_2 \frac{p(x_i|R_j)}{p(x_i)}, \tag{16}$$

and it still follows relation (11). It is worth to mention that the AMI linking X and R, $I(X;R)$, is related to a specific decision rule at the receiver end, i.e., how we specify R_j's. It is also possible to define an AMI linking X and Y, $I(X;Y)$, that is independent of a certain decision rule following the continuous distribution nature of Y in a noisy channel. Both $I(X;R)$ and $I(X;Y)$ are of interest to analyze the communication system performance. The AMIs represent the potential capacity of

a communication system under a given source probability assignment, i.e., $p(x_i)$'s, and certain channel characteristics. In the following, we adopt $I(X;R)$ to characterize the AMI of a noisy communication system under specific decision rules to guide practical applications.

As discussed in Subsection 3.1, in a noiseless system, $H(Y|X)$ is equal to 0. However, in the presence of noise and with a specific source configuration, the event R becomes uncertain. As a result, the quantity $H(R|X)$ will have a non-zero value. Therefore, based on formula (11), the average mutual information of noisy systems under the same source code selection strategy will be lower than that of the noiseless system. As an example, for a noisy DDM system with observations conducted along the direction $\theta = 45^\circ$ $\phi = 0^\circ$, if the same code selection strategy is used as the constructed one-to-one correspondence machanism discussed in Section 3.2, the AMI following Eq. (16) is calculated as 2.21 bit for a 20 dB SNR which is considerably smaller than the noiseless AMI, which is just the source entropy $H(X) = 6.91$ bit as shown in Table 2. Even if the SNR is increased to 30 dB, the AMI only reaches 3.35 bit for $I(X;R)$. Obviously, under such coding scheme and noise level, information transmission cannot be carried out efficiently. Therefore, a better source coding strategy needs to be implemented.

TABLE 2. Entropy, AMI/JAMI and capacity for single and joint observations with various noise levels and coding strategies.

Observation directions	Noise level	Coding strategy	$H(X)$	AMI/ JAMI	C
$\theta = 45^\circ$, $\phi = 0^\circ$	No	all codes	16	5.47	6.91
		codes with all y_i's	6.91	6.91	
	SNR= 20 dB	codes with all y_i's	6.91	2.21	2.45
		code selection $d/\sigma = 4$	2.32	1.94	
	SNR= 30 dB	codes with all y_i's	6.91	3.35	3.67
		code selection $d/\sigma = 4$	3.59	3.36	
$\theta = 45^\circ$, $\phi = 0^\circ$ and $\theta = 54^\circ$, $\phi = 72^\circ$	No	all codes	16	5.47	13.66
		codes with all y_i's	13.66	13.66	
	SNR= 20 dB	code selection $d/\sigma = 4$	4.7	3.54	3.54- 13.66
	SNR= 30 dB	code selection $d/\sigma = 4$	7.14	6.34	6.34- 13.66

In the following, we propose an alternative source code selection scheme to improve the DDM communication system performance, and the decision rule in the receiver still follows Eq. (14) to obtain corresponding receiving events. Note that the code selection method presented herein is practical and relatively superior, although it is not necessarily deemed as the strictly optimal solution.

1. All the possible noiseless far field values are sorted from smallest to largest, i.e., y_j, j from 1 to N_y as discussed in Subsection 2.2.2.

2. y_1 is selected as the first selected noiseless receiving value, and the smallest RIS code in $A_x(y_1)$ is chosen as the first selected source code. Recall that $A_x(y)$ is defined as the set of source codes with the same observation value y as described in Eq. (7).

3. Select the next noiseless receiving value y, which is the nearest scattering field value that differs from the previous selected noiseless receiving value greater than $d = 4\sigma$. And the smallest RIS code in $A_x(y)$ is chosen as the next selected code. d is the difference value of the selected two adjacent receiving far-fields[3]. Furthermore, the impact of d will be discussed following in this subsection.

4. This procedure is repeated to produce all the selected codes.

5. These chosen codes are then assigned equal probability distribution.

Following this method, the number of selected codes under 20 dB SNR is 5 (with hardware code number of 248, 305, 2033, 4100, and 13108, respectively) for observation in $\theta = 45$ $\phi = 0^\circ$, as illustrated in Fig. 6(a), where the solid lines are the corresponding receiver event boundaries (decoding boundaries) under our code selection strategy. The corresponding source entropy and AMI are 2.32 and 1.94 bits, respectively. For observation in $\theta = 13.5^\circ$ $\phi = 36^\circ$, the source entropy and AMI are 2.81 and 2.37 bit, respectively. After the code selection process, the transmission rate is decreased, but the transmission quality has been significantly improved as the AMI approaches the source entropy $H(X)$.

It is expected that adjusting d in the code selection rule balances the information carrying capability and decoding noise. In Fig. 9, the source entropy and AMI under different source selection rules for observation in $\theta = 45^\circ$ and $\phi = 0^\circ$ are reported. It can be seen that as d increases, the number of the selected codes decreases, and thus the source entropy decreases, eventually converging toward the AMI. It is interesting to note that AMI exhibits a weak convex dependence with respect to d/σ. This can be explained by the fact that the AMI is upper-bounded by both the source entropy and the signal to noise ratio (SNR) at the receiver. The SNR relates to the distinguishability of the signal at the receiver end. These relations are embodied in the results shown in Fig. 9. When d/σ is small, i.e., the source entropy is large, the AMI is largely connected to SNR and thus does not change much. When d/σ becomes large, i.e., the source entropy decreases, the AMI is largely linked to and

[3] The variable d is adjustable in the code selection process, which will affect the information carrying capability and the decoding accuracy. In this article, we have selected the rule $d = 4\sigma$, which corresponds to a 95.44% (using the 2σ principle) assurance that the received value will fall within the correct judgment range.

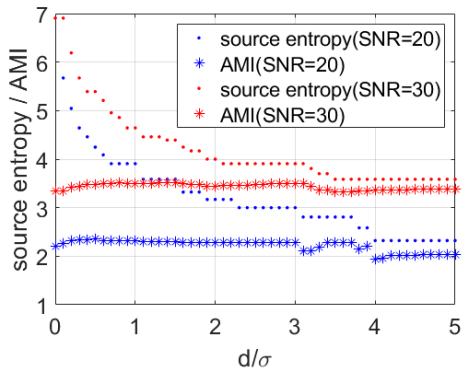

FIGURE 9. Source entropy and AMI against d/σ in the source code selection rules observed in $\theta = 45°$ $\phi = 0°$.

limited by the source entropy. On the other hand, the source entropy reaches a staircase decreasing pattern with a larger d/σ due to the clustered distribution nature of the scattering field values, as indicated in Fig. 6. Thus a relatively larger d/σ might be desired to reduce the error of the symbol decision made at the receiver side while not decreasing the AMI significantly. The analysis above shows that different noise levels and code selection strategies severely affect the information handling capacity of the DDM system. Table 2 summarizes the source entropy and average mutual information for several different observation noise and coding settings. The capacity for each observation and noise configuration is also reported. The concepts of joint AMI (JAMI) and capacity are to be discussed as follows. It can be seen by comparing the difference of AMI and entropy that the presence of noise hinders the information transmission capability of proposed DDM system, while the code selection strategies facilitate an improved performance.

3.4. Information Transmission Experiment: A Simulation

To demonstrate the performance of the DDM prototype with the proposed code selection strategy in a noisy environment, a simulated transmission experiment was conducted transmitting an example image with a procedure as illustrated in Fig. 10. The

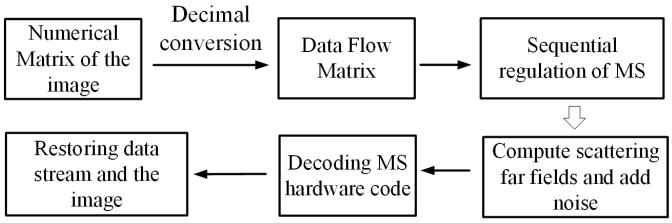

FIGURE 10. Flowchart depicting the experimental process of image transmission utilizing the DDM system.

test image (Fig. 11(a)) is with a size of 531k bytes. The observation direction was set to $\theta = 13.5°$ and $\phi = 36°$. Based on the code selection strategy described in Section 3.3 with $d/\sigma = 4, 7$ hardware codes with code numbers 9, 54, 570, 577, 686, 1871, and 26514 are selected for a 20 dB SNR noise setting, and the decoding boundaries are shown in Fig. 6(b). During the transmission process, the information stream of each image frame, i.e., the 8-bit binary gray value of each pixel, was converted to a 3-bit septenary form. For instance, '215' was treated as '425', and the hardware codes for the metasurface were coded in the order of 577, 54, and 686 to transmit the information. The image received under a system with 20 dB SNR is displayed in Fig. 11, and it shows clear recovery to the original image. However, the same coding strategy used in a system with 10 dB SNR and a system with 5 dB SNR resulted in vague images, as shown in Fig. 11(c) and (d), respectively, indicating the need for more effective code selections. The corresponding bit/symbol error rates (BER) as evaluated on the septenary digits are 0.0328, 0.0409, and 0.3859, respectively, for the three SNR settings. These characteristics are summarized in Table 3 (Cases for joint observation will be discussed following in Section 4.3). This observation is also supported by the comparison of the AMI and source entropy. In the 20 dB system, the source entropy and AMI are 2.81 and 2.37 bits, respectively, which are close to each other. However, for the 10 dB and 5 dB systems, if the same coding strategy is applied, the resulting AMIs are 1.14 and 0.56 bits, respectively, which are much lower than the source entropy of 2.81 bits, leading to higher bit error ratios. Therefore, the significance of the proposed parameters in the analysis of the coding strategies of the DDM system is clearly demonstrated.

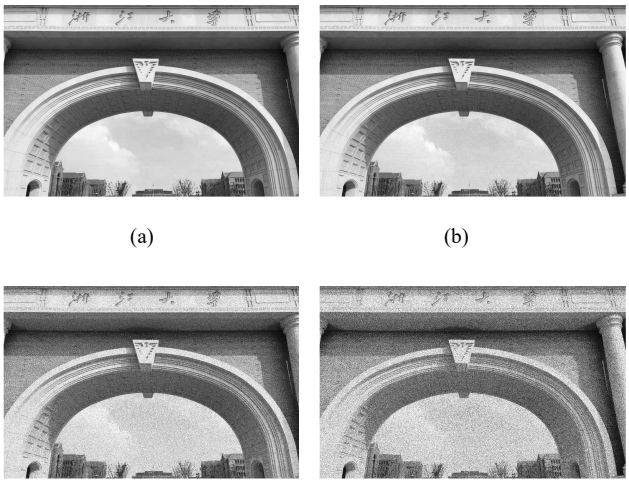

(a) (b) (c) (d)

FIGURE 11. Simulation experiment of the DDM communication system. The hardware codes are selected with $d/\sigma = 4$ and a 20dB SNR assumption. (a) Image to be transmitted. (b) The received image under a 20 dB SNR. (c) The received image under a 10 dB SNR. (d) The received image under a 5 dB SNR.

4. AVERAGE RECEIVER MUTUAL INFORMATION AND JOINT OBSERVATIONS

4.1. Average Receiver Mutual Information

Compared to single-point observation schemes, in DDM systems, a joint observation strategy that simultaneously observes two or more points in the far-field zones is expected to increase the information handling capacity, but at the cost of increased

TABLE 3. Entropy, AMI, and BER at different noise levels under the same code selection strategy. (The fixed code selection strategy is obtained in a 20dB SNR system with $d/\sigma = 4$.) The single observation direction is $\theta = 13.5°$, $\phi = 36°$; The joint observation directions are $\theta = 45°$, $\phi = 0°$ and $\theta = 54°$, $\phi = 72°$.

SNR	Entropy (Single)	AMI	BER	Entropy (Joint)	JAMI	BER
20 dB	2.81	2.37	0.0328	4.7	3.54	0.0711
10 dB	2.81	1.14	0.0409	4.7	1.82	0.3204
5 dB	2.81	0.56	0.3859	4.7	0.89	0.5007

complexity and cost. Here, we first investigate the degree of correlation between different far-field directions under a specific source coding strategy.

To express the correlation degree of different observation directions, considering two receiving directions O_y and O_z with observation values y and z, we define the average receiver mutual information (ARMI) as,

$$I(Y;Z) = \sum_{j=1}^{N_z}\sum_{i=1}^{N_y} p(z_j)\, p(y_i|z_j) \log_2 \frac{p(y_i|z_j)}{p(y_i)}. \quad (17)$$

To compute $p(y_i|z_j)$, we use $A_x(z_j)$, which is defined as in Eq. (7), in order to express the set of source codes in terms of the same observation value z_j. Similarly, $A_x(y_i, z_j)$ is deployed to capture the source codes set corresponding to scattering far-field values y_i and z_j along the chosen two observation directions. Consequently, we may write,

$$\begin{aligned} p(y_i|z_j) &= \frac{p(y_j, z_i)}{\sum_{m=1}^{N_x} p(x_m) p(z_j|x_m)} \\ &= \frac{\sum_{m=1}^{N_x} p(y_i, z_j|x_m)}{\sum_{m=1}^{N_x} p(z_j|x_m)} \\ &= \begin{cases} \frac{C[A_x(y_i,z_j)]}{C[A_x(z_j)]}, & A_x(y_i, z_j) \neq \varnothing, \\ 0 \quad\quad\quad\quad , & A_x(y_i, z_j) = \varnothing, \end{cases} \end{aligned} \quad (18)$$

where the third equal sign follows from the assumption of equal probability of each source code. The measure ARMI in (18) provides information about the eliminated average uncertainty for the information in O_y from the observation in O_z direction; thus, it describes the correlation between two different observation directions. A larger ARMI indicates smaller mutual independence between two observations, while a smaller one represents a weaker correlation. When choosing another joint observation direction for improving the observation capability, we shall select the direction with a small ARMI, for locations with small correlations can provide more information for the source. Still, taking the 4×4 metasurface DDM system with 16 bit equi-probability encoding as an example, we choose the direction $\theta = 45°$, $\phi = 0°$ as the O_y direction, and the ARMI in different O_z directions can be calculated as shown in Fig. 12

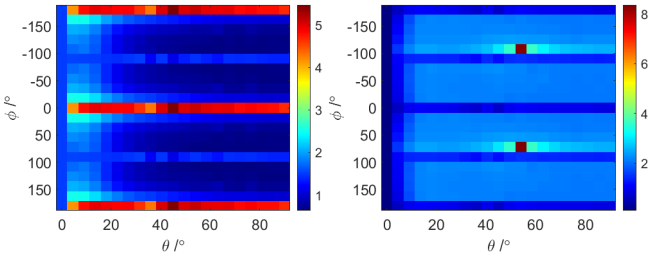

(a) (b)

FIGURE 12. ARMI for a 4×4 metasurface DDM system. (a) y in $\theta = 45°$, $\phi = 0°$. (b) y in $\theta = 54°$, $\phi = 72°$.

(a). It can be seen then that ARMI is larger at directions having the same or symmetrical ϕ with respect to the O_y direction, which implies the presence of a high degree of correlation between these directions and O_y.

4.2. Joint Observations for Noiseless Systems

As stated earlier, if all available transmitting binary codes were to be used for sending information from an information source whose entropy is 16 bit, a single-point observation along $\theta = 45°$, $\phi = 0°$ can only reach a 5.47 bit AMI as there are different transmitting binary source patterns eventually leading to the same far-field observation value. If multiple observation directions are applied, more source code patterns may be separated due to the introduction of independent observations. This simple concept is associated with the increasing AMI with more observation directions. It is possible for the AMI to approach the source entropy with enough independent observations. The measure of the joint average mutual information (JAMI) is introduced to quantitatively evaluate the information transmission capability of the DDM system under joint observations, by generalizing Eq. (10). While the JAMI shares the same physical significance as AMI, the main difference is that the receiver value becomes a vector composed of observations at multiple directions. The JAMI $I(X;Y,Z)$ associating source X and two independent observations Y and Z is defined as follows,

$$I(X;Y,Z) = \sum_{j=1}^{N_{(y,z)}}\sum_{i=1}^{N_x} p(x_i)\, p[(y,z)_j|x_i] \log_2 \frac{p[x_i|(y,z)_j]}{p(x_i)}, \quad (19)$$

where $(y,z)_j$ represents the jth observation value combination, while $N_{(y,z)}$ is the number of far-field observation values obtained for the joint measurement at the directions associated with y and z. The JAMI $I(X;Y,Z)$ can be further generalized to handle more than two observation directions.

In order to illustrate the significance of JAMI, we provide an example where all transmitting metasurface patterns (hardware codes) are assumed equi-probable. The JAMI of a DDM system is evaluated and reported in Table 4 with a fixed observation O_y along $\theta = 45°°$, $\phi = 0°°$ and a varying direction O_z along three different angular directions z_1 ($\theta = 45°, \phi = -180°$),

z_2 ($\theta = 22.5°, \phi = -90°$), and z_3 ($\theta = 54°, \phi = -72°$), repectively.

as shown in Table 4. The correlation degree between those three O_z directions with the O_y direction can be described by the ARMI as defined in Section 4.1, whose value is shown in the third column of Table 4. Calculations confirm that joint observations with smaller ARMI directions are associated with a larger JAMI. The AMI increases to a higher value of 13.17 bit for joint observations in $\theta = 45°$, $\phi = 0°$ and $\theta = 54°$, $\phi = 72°$. We can further calculate the ARMI between other locations with $\theta = 54°$, $\phi = 72°$ as shown in Fig. 12(b). Combining with Fig. 12(a), we may select another angular sector $\theta = 63°$, $\phi = 108°$ that has small ARMI with both $\theta = 45°$, $\phi = 0°$ and $\theta = 54°$, $\phi = 72°$. This is a direction that provides relatively independent observations to the source compared to the other two chosen directions. The JAMI combining all these three directions reaches 14.28 bit, which is quite close to the source entropy. This indicates that it is possible to select an optimum or near-optimal set of directions for a specialized programmable DDM joint observation scheme whose combined JAMI can be sufficiently close to the source entropy.

TABLE 4. JAMI and ARMI for joint observations.

Cases	AMI for x	ARMI with y	JAMI for x
y: only $\theta = 45°$ $\phi = 0°$	5.47	/	/
with z_1: $\theta = 45°$ $\phi = -180°$	5.47	5.46	5.48
with z_2: $\theta = 22.5°$ $\phi = -90°$	6.33	1.44	10.35
with z_3: $\theta = 54°$ $\phi = 72°$	8.36	0.66	13.17

The above analyses are based on applying ARMI measures to select observation directions for better information transmission and processing capabilities. On the other hand, when the observation directions are given, one can select the source codes following a similar strategy as mentioned in Subsection 3.2 originally presented for the single observation scenario. The purpose is to establish a one-to-one correspondence between the source code transmitting pattern on one end, and the observation field vector on the other end, with the final objective to satisfy the information-theoretic requirement that the AMI and the source entropy be as close to each other as possible for an effective transmission over noiseless channels. Taking joint observations along $\theta = 45°$, $\phi = 0°$ and $\theta = 54°$, $\phi = 72°$ as an example, the number of selected coding is 12901 with a source entropy and JAMI of 13.66 bits. This calculation demonstrates a significant improvement over the single-observation scenario whose corresponding source entropy and AMI is only 6.91 bits. The results are summarized in Table 2.

4.3. Noisy Joint Observation Schemes for DDM Systems and Optimized Codes

We then consider the code selection process for a noisy system with two joint observations at O_y and O_z. Let us again assume an additive Gaussian noise superimposed on both observation directions, and we use the average field magnitude at direction O_y as the reference in defining the SNR. The decision boundaries on the y and z observation plane are determined by applying the strategy as developed in Subsection 3.3 twice. First, we apply the same hardware code selection strategy for the single observation scenario (Subsection 3.3) in order to compute the received signal y's decision region boundaries. Next, for the codes falling within each subdomain of a y decision region, we employ the strategy again to obtain the decision boundaries associated with the received (observed) signal z. These decision boundaries are illustrated in Fig. 13 as solid lines with $d/\sigma = 4$. Finally, the hardware code whose far-field observation value is closest to the center of each rectangular subdomain is chosen as a selected code. Following this strategy, a 20 dB SNR system has a source entropy of 4.70 bits and a JAMI of 3.54 bits. If the SNR is increased to 30 dB, an improved communication capability with source entropy of 7.14 bits and JAMI of 6.34 bits is obtained. These values are also included in Table 2 for comparison. The source entropy and AMI/JAMI for both single observation and joint observation scenarios performed after code selections are shown in Fig. 14 against varying noise levels. It is clear that the joint observation scenario is linked to a higher mutual information transfer capability compared to the single observation case. It is also noted that under a given noise level, the absolute difference between the JAMI and the entropy $H(X)$ for the joint observation case is larger than that between the AMI and $H(X)$ for the single observation case. This is due to the increased constellation density in the observation plane and the associated increase in decision errors.

A numerical experiment is also constructed to demonstrate the proposed code selection strategy and the significance of the

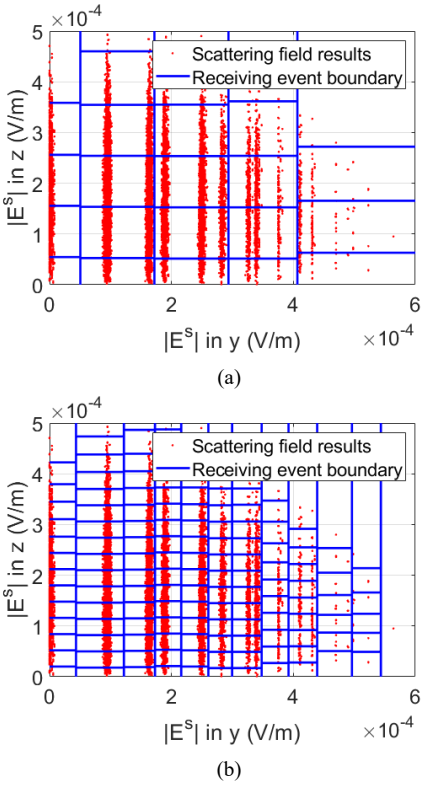

FIGURE 13. Code optimization boundaries overlaid on the 2D scattering field plot observed in directions $O_y(\theta = 45°, \phi = 0°)$ and $O_z(\theta = 54°, \phi = 72°)$. (a) SNR = 20 dB. (b) SNR = 30 dB.

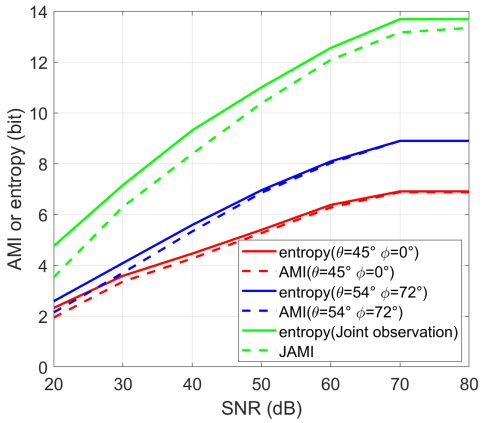

FIGURE 14. Noisy system AMI and entropy for single observations and joint observation after source code selections.

proposed parameters under joint observations extending the example discussed in Subsection 3.4. The observation directions are assumed in $\theta = 45°$, $\phi = 0°$ and $\theta = 54°$, $\phi = 72°$, and a system with SNR of 20 dB is considered. A code selection with $d/\sigma = 4$ leads to 26 available hardware codes, much larger than 7 for the single observation case. The transmission experiment yields the received image as shown in Fig. 15(b), illustrating good transmission quality with a JAMI of 3.54 bit, an entropy of 4.7 bit, and a bit error rate (BER) of 7.11%, respectively. These statistics are summarized in Table 3. The larger JAMI versus the AMI indicates an improved transmission efficiency as compared to the single observation scheme discussed in Subsection 3.4.

Table 3 also compiles the characteristics to transmit the image following the joint observation scheme with the same set of hardware codes and decision rules while the SNR is decreased to 10 dB and 5 dB, respectively. The corresponding transmitted images are illustrated in Fig. 15 (c) and (d), respectively. The achieved JAMI's are only 1.82 bit and 0.89 bit, respectively, much less than the source entropy. The corresponding BERs are large of 32.04% and 50.07%, respectively, consistent with the blurred images received. The BERs for the joint observations are much larger than those for single observations, (i.e., 4.09% and 38.59%, respectively, for SNRs of 10 dB and 5 dB, cf. Table 3) accompanying relatively larger differences between the source entroy and the JAMI/AMI's.

5. CHANNEL CAPACITY

5.1. Channel Capacity for Noiseless Systems

The AMI and JAMI described above provide quantitative assessment of the level of the information transmitted along one or more directions under a given coding strategy. The maximum amount of information that a channel can transmit, i.e., the channel capacity, is another fundamental parameter [51] to guide the choice of observation directions and settings for higher transfer capabilities [2]. In the DDM system presented, the Shannon information capacity can be defined as the maximum value of AMI optimized over all possible a priori probability distributions assigned to the digital source codes. From

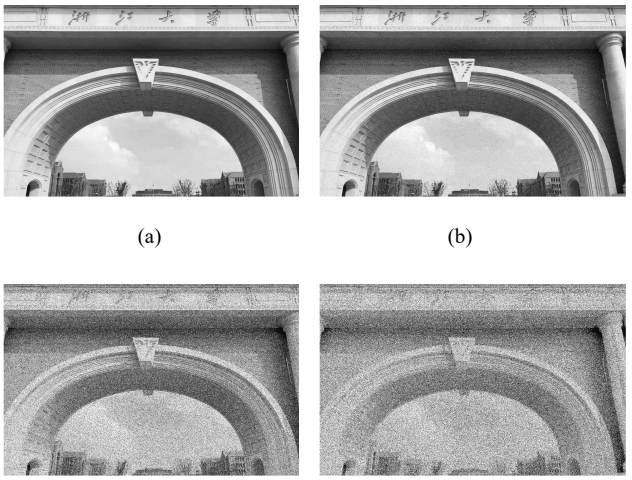

(a) (b)

(c) (d)

FIGURE 15. Simulation experiment of the DDM communication system under joint observation. (a) Image to be transmitted. (b) The received image under a 20 dB SNR with 20 dB SNR code selection strategy. (c) The received image under a 10 dB SNR with 20 dB SNR code selection strategy. (d) The received image under a 5 dB SNR with 20 dB SNR code selection strategy.

the aforementioned analysis, the AMI of a noiseless DDM system is equal to its receiver entropy $H(Y)$. Its channel capacity C then follows [2, 51, 60]

$$C = \max_{p(y_i)} H(y) = \max_{p(y_i)} \sum_{i=1}^{N_y} \left[-p(y_i)\log_2 p(y_i)\right]. \tag{20}$$

The capacity C, i.e., the maximum entropy $H(y)$, is achieved with a uniform distribution of y_i and a maximum N_y, following the maximum entropy theorem [60], giving rise to $C = \log_2 N_y$. For the DDM system presented, N_y, and thus C, varies with the choice observation direction and the metasurface complexity. The directional patterns of C for a 3×3 and 4×4 metasurfaces are shown in Fig. 16. The channel capacity of the 4×4 metasurface is consistently higher than that of the 3×3 system due to a higher degree of source patterning freedom. The directional patterns of C is related to the symmetry of the observation direction in the frame of the metasurface placement. Some observation directions are corresponding to richer

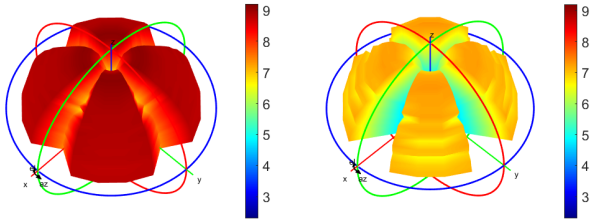

(a) (b)

FIGURE 16. Capacity distributions for noiseless system. (a) 4×4 metasurface. (b) 3×3 metasurface.

sets of scattering field diversities. This is also evident in Fig. 6 as we compare the scattering field statistics at two chosen directions. The maximum value of the capacity over all possible observation directions, $C_{\max}$, is defined to characterize the maximal information carrying capability of the metasurface, and it amounts to 7.33 and 9.11 bits for the 3×3 and 4×4 metasurfaces, respectively. To characterize the overall information carrying capability of the metasurface over all possible directions, the capacity C can be averaged over the half-space of the solid angle to yield an average capacity C_{ave}, which amounts to 6.17 and 8.23 bits for the 3×3 and 4×4 metasurfaces, respectively. It is always of interest to define the maximum capacity per unit area of the metasurface, $\tilde{C}_{\max}$, and the average capacity per unit area of the metasurface, $\tilde{C}_{\text{ave}}$, to characterize the information carrying capability per unit area of the reconfigurable metasurface, which amounts to 16623.4 and 13988.8 bits/m^2 for $\tilde{C}_{\max}$, and 11614.7 and 7868.7 bits/m^2 for $\tilde{C}_{\text{ave}}$, for the 3×3 and 4×4 metasurfaces, respectively. The unit cell size of the metasurface is taken as 7 mm $\times$ 7 mm as described in Section 2.1. These characteristics are also summarized in Table 5. It is noted that a lager metasurface exhibits an increased average capacity, yet its efficiency represented by the average capacity per unit area diminishes.

TABLE 5. The maximum capacity, average capacity, maximum capacity per unit, and average capacity per unit for 3×3 and 4×4 metasurfaces under noiseless and noisy system. The maximum and average operator is managed over the half-space of the solid angle. A decision rule derived with $d/\sigma = 4$ is in use for the noisy system.

MS	Noise	$C_{\max}$ (bits)	C_{ave} (bits)	$\tilde{C}_{\max}$ (bits/m^2)	$\tilde{C}_{\text{ave}}$ (bits/m^2)
3×3	No	7.33	6.17	16623.4	11614.7
	30 dB	3.27	2.86	7422.7	6486.4
	20 dB	1.87	1.54	4236.6	3498.9
4×4	No	9.11	8.23	13988.8	7868.7
	30 dB	4.14	3.76	5284.1	4791.9
	20 dB	2.64	2.32	3362.2	2957.7

We also examine the effects of metasurface element size on the capacity characteristics. The capacity parameters $C_{\max}$, C_{ave} are plotted versus the metasurface element size in Fig. 17(a) for a 3×3 and 4×4 metasurface, respectively, while the capacity parameters $\tilde{C}_{\max}$ and $\tilde{C}_{\text{ave}}$ are illustrated in Fig. 17(b). It is noted that a larger element size associates with a higher capacity and a reduced capacity per unit area. These observations are linked to the physical scattering characteristics of the metasurface, highlighting the necessity to combine electromagnetic scattering analysis and the information characterization. Note that in practice, the chosen metasurface element size must follow the physical requirement in designing the reconfigurable metasurface with desired scattering properties [33, 44]. In this paper, we have assumed that the PO assumption of formula (2) holds valid for the range of the metasurface element sizes being investigated. The details in tuning the metasurface structure to meet the phase change properties are beyond the scope of this paper.

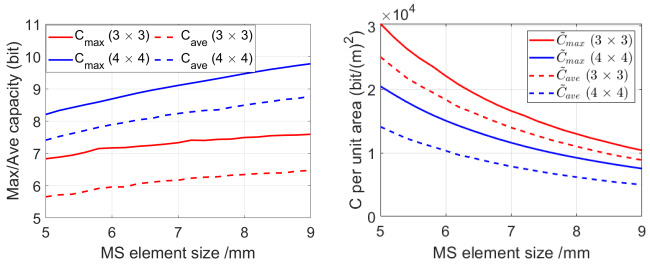

FIGURE 17. (a) Average/Maximum capacity under different metasurface element size. (b) Average/Maximum capacity per unit area under different metasurface element size.

The channel capacity C defined in Eq. (20) for a single observer in a noiseless system is ready to be generalized to handle joint observations in a noiseless environment. The channel capacity of the 4×4 metasurface with joint observations at a fixed direction of $\theta = 54°$, $\phi = 72°$ and a varying second direction is illustrated in Fig. 18. It is overall larger than that derived from a single observer at the fixed direction. It is also noted from Fig. 18 that the joint observation capacity is lower at directions having the same or symmetrical ϕ with respect to the fixed direction. This is attributed to the high degree of correlation in those directions, as demonstrated in Subsection 4.1 and Fig. 12. Therefore, such highly correlated directions shall be avoided in practical configuration of joint observations with the aim to improve capacity.

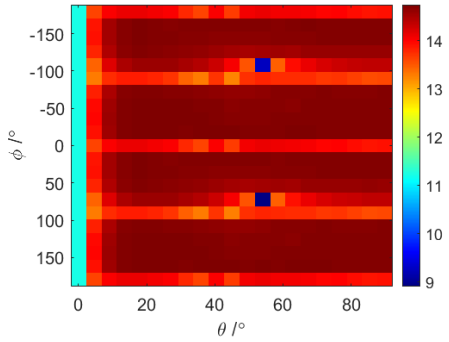

FIGURE 18. The capacity of joint observations at two directions including a fixed direction of $\theta = 54°$, $\phi = 72°$ and another direction.

5.2. Channel Capacity for Noisy Systems

To compute channel capacity with noise given a set of receiving events R_j's corresponding to the selected code x_j's, let us introduce a transition probability matrix P, considering the discrete nature of the DDM system,

$$P = \begin{bmatrix} p(R_1|x_1) & p(R_2|x_1) & \cdots & p(R_{N_R}|x_1) \\ p(R_1|x_2) & p(R_2|x_2) & \cdots & p(R_{N_R}|x_2) \\ \cdots & \cdots & \cdots & \cdots \\ p(R_1|x_{N_R}) & p(R_2|x_{N_R}) & \cdots & p(R_{N_R}|x_{N_R}) \end{bmatrix} \quad (21)$$

where $p(R_j|x_i)$ is the transition probability from the ith input to the jth receiving event. For a channel with an invertible transition probability matrix, we apply the channel capacity theorem and the Bluhat-Arimoto iterative algorithm to obtain its channel capacity [60, 61]. The capacity is reached when the $p(x)'s$ are arranged such that the following conditions are satisfied per the channel capacity theorem,

$$I\left(X = x_i; R\right) = C, \ \forall\, p\left(x_i\right) > 0, \tag{22}$$

$$I\left(X = x_i; R\right) \leq C, \ \forall\, p\left(x_i\right) = 0, \tag{23}$$

where C is the channel capacity, and

$$I\left(X = x_i; R\right) = \sum_{j=1}^{N_y} p(R_j|x_i) \log \frac{p(R_j|x_i)}{p(R_j)} \tag{24}$$

is the average mutual information between a single symbol x_i and the receiving event R.

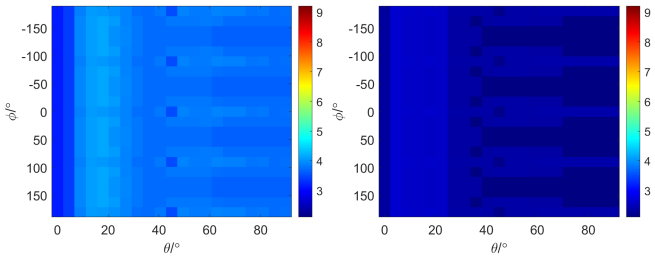

(a) (b)

FIGURE 19. Capacity for noisy systems. The structure of metasurface is 4×4. (a) 30 dB SNR. (b) 20 dB SNR.

Figure 19 shows the angular distribution of such estimated channel capacity for a 4×4 metasurface in a system with 30 dB SNR and 20 dB SNR, respectively, following the code selection strategy discussed in Subsection 3.3. The directional averaged channel capacity, C_{ave}, amounting to 3.76 bit and 2.32 bit for the two noise levels, respectively, is much lower than that of the noiseless system, 8.23 bit, as depicted in Fig. 16(a). The maximum channel capacity, C_{max}, amounting to 4.14 bit and 2.64 bit, respectively, is also much lower than that of the noiseless system, 9.11 bit. These characteristics are also summarized in Table 5. Furthermore, comparing with Fig. 16, it is noted that the angular distribution of the channel capacity becomes more uniform as SNR decreases, a result of the more uniform distribution of the far fields and less decision boundaries.

In a noisy communication environment, it is of interest to compare the channel capacity and the achieved AMI/JAMI under a specific coding strategy. A coding strategy represents a specific set of $p(x)$'s being assigned to the hardware source patterns. Following definition, the AMI will be upper-bounded by the capacity (C). For an effective communication system, we expect the achieved AMI approaching the capacity, implying that the channel capacity is fully exploited, while the AMI and capacity approach the source entropy corresponding to the deployed $p(x)$'s, indicating a lower error rate of information transmission. These are illustrated in Table 2 by comparing the AMI and the source entropy corresponding to the equal-probable $p(x)$'s coding strategy and the channel capacity. The obtained AMI after source code selection is near the capacity, and it also approaches the entropy, indicating the effectiveness of the strategy. The same set of relations are utilized to estimate the ranges of the capacity C for the joint observation scenarios, where rigorous calculation becomes difficult due to the substantially expanded degrees of freedom.

6. CONCLUSIONS

This study provided a comprehensive investigation into electromagnetic information characterization techniques in the context of RIS-enabled DDM communication systems where a conventional linear channel matrix **H** based analyzing method would fail. To this end, we introduced four key parameters, namely AMI, ARMI, JAMI, and channel capacity, established their relationship with the scattering characteristics of the metasurface, and demonstrated these relations and the behavior of the parameters. We also examined the efficacy of different coding strategies for information transmission in scenarios involving single or multiple observations, and with or without noise.

Our investigation of RIS used in DDM systems yielded several noteworthy findings. We established that AMI can effectively capture the average observation capability of a particular direction for a given coding strategy. The ARMI is proved to be an effective measure of the correlation of observations across different directions. Our results suggest that directions with low ARMI values can be jointly taken to enhance the quality of information transfer, as compared to single observations. Our study underscored the significance of code selection in satisfactory DDM system operation for practical information processing and transmission. These findings provide valuable insights into the design and implementation of RIS-enabled DDM communication systems, with potential implications for future research in this field. While noise degrades communication system performance, proper code selection strategy improves communication reliability and accuracy. We established that the channel capacity of the RIS-enabled DDM communication system can be estimated using the receiver entropy for a noiseless system or the transition probability matrix for a noisy system under a specific decision rule. Our analysis further revealed that the channel capacity is significantly influenced by multiple factors, including the observation directions, metasurface element numbers and cell sizes, configuration of joint observations, and noise levels. These findings suggest that optimization of the information system performance can be achieved by appropriately configuration of all these parameters. Relations among the source entropy, AMI/JAMI, and channel capacity are also illustrated as performance indicators of a practical communication system.

The developed approach enables us to gain insights into the behavior of the novel DDM system under varying conditions, facilitating the design and implementation of efficient and reliable communication systems. It is worth noting, however, that accurately analyzing the electromagnetically-aware statistics of joint observation scenarios requires significant computational resources owing to the large number of degrees of free-

dom involved. Nonetheless, by leveraging appropriate computational tools and techniques, such as machine learning and optimization algorithms, these challenges can be potentially addressed. It is also noteworthy that much of the analysis carried in this paper is in its primitive stage. The purpose of the paper is more on presenting EM information characterization of scattering reconfigurability enabled information system as an emerging new field to the audience with interest. Much is yet to be done: a more rigorous characterization of noise, environment, and channel fluctuation on the system performance is desired; more accurate EM scattering analysis of the RIS scattering, fully incorporating the near fields and polarization effects, is on the way to clarify its impact on the information metrics; multiple variants of the DDM systems, including high degree-of-freedom RISs and continuous controllable RISs, are being designed and to be analyzed and optimized in terms of their information characteristics; a theoretical interpretation for the spatial distribution of communication capacity in the RIS-DDM system, especially through the spatial harmonic analysis is desired. We believe that the insights gained from our study hold significant promise for advancing the field of information metasurface-enabled communication systems, as well as other areas of electromagnetic information processing and transmission. Our proposed parameters and approaches offer insights for designing and analyzing RIS-enabled DDM systems, and can be extended to other EM information systems.

ACKNOWLEDGEMENT

This work was supported by the Major Research Instrument Development Program of National Natural Science Foundation of China (62027805), the National Natural Science Foundation of China (61901411), and the startup funds of Zhejiang University. TJC acknowledges the supports from the Basic Scientific Center of Information Metamaterials of the National Natural Science Foundation of China (6228810001), the National Key Research and Development Program of China (2017YFA0700201, 2017YFA0700202, 2017YFA0700203), and the Major Project of Natural Science Foundation of Jiangsu Province (BK20212002).

APPENDIX A. PROOF OF THE ML DETECTOR CONDITION FOR THE DDM SYSTEM

The ML detector of the system is given by,

$$\widehat{x} = \arg\max_{x\in C_x} p(y|x) = \arg\min_{x\in C_x} |y - f(x)|^2, \qquad \text{(A1)}$$

where, C_x is the set of all possible realizations of x, while y is the receiving value. For any specific source x_p, and its corresponding receiving value $y_j = f(x_p)$, the value $|y - f(x_p)|^2$, or equivalently $|y - y_j|^2$, achieves its minimum when the following conditions are met:

$$|y - y_j|^2 < |y - y_{j+1}|^2 \text{ and } |y - y_j|^2 < |y - y_{j-1}|^2 \qquad \text{(A2)}$$

where, y_{j+1} and y_{j-1} represent the larger and smaller possible receiving values adjacent to y_j. The solution to these conditions is finally given by,

$$\frac{y_j + y_{j-1}}{2} < y < \frac{y_j + y_{j+1}}{2}. \qquad \text{(A3)}$$

REFERENCES

[1] Ishimaru, A., *Wave Propagation and Scattering in Random Media*, Oxford University Press, New York, 1997.

[2] Lathi, B. P. and Z. Ding, *Modern Digital and Analog Communication Systems*, Oxford University Press, New York, 2019.

[3] Coskun, V., B. Ozdenizci, and K. Ok, "A survey on near field communication (NFC) technology," *Wireless Personal Communications*, Vol. 71, 2259–2294, 2013.

[4] Franceschetti, M., M. D. Migliore, P. Minero, and F. Schettino, "The information carried by scattered waves: near-field and nonasymptotic regimes," *IEEE Transactions on Antennas and Propagation*, Vol. 63, No. 7, 3144–3157, 2015.

[5] Chandra, K., R. V. Prasad, and I. Niemegeers, "An architectural framework for 5G indoor communications," in *2015 International Wireless Communications and Mobile Computing Conference (IWCMC)*, 1144–1149, Dubrovnik, Croatia, 2015.

[6] Lai, H. W., K.-M. Luk, and K. W. Leung, "Dense dielectric patch antenna — a new kind of low-profile antenna element for wireless communications," *IEEE Transactions on Antennas and Propagation*, Vol. 61, No. 8, 4239–4245, Aug. 2013.

[7] Mikki, S. M. and Y. Antar, "Unifying electromagnetic and communication theories: A proposal for a new research program," in *2016 URSI International Symposium on Electromagnetic Theory (EMTS)*, 435–438, 2016.

[8] Migliore, M. D., D. Pinchera, M. Lucido, F. Schettino, and G. Panariello, "An electromagnetic analysis of noise-based intrinsically secure communication in wireless systems," *Electronics*, Vol. 7, No. 7, 113, 2018.

[9] Mikki, S. and Y. Antar, *New Foundations For Applied Electromagnetics: The Spatial Structure of Electromagnetic Fields*, Artech House, 2016.

[10] Tulino, A. M., A. Lozano, and S. Verdu, "Impact of antenna correlation on the capacity of multiantenna channels," *IEEE Transactions on Information Theory*, Vol. 51, No. 7, 2491–2509, 2005.

[11] Gruber, F. K. and E. A. Marengo, "New aspects of electromagnetic information theory for wireless and antenna systems," *IEEE Transactions on Antennas and Propagation*, Vol. 56, No. 11, 3470–3484, 2008.

[12] Zhang, Z. and L. Dai, "Continuous-aperture MIMO for electromagnetic information theory," *Arxiv Preprint Arxiv:2111.08630*, 2021.

[13] Miller, D. A. B., "Waves, modes, communications, and optics: A tutorial," *Advances in Optics and Photonics*, Vol. 11, No. 3, 679–825, 2019.

[14] Mikki, S. and A. Hanoon, "Spectral efficiency enhancement using an antenna-based orthogonal frequency division multiaccess technique," *International Journal of RF and Microwave Computer-aided Engineering*, Vol. 30, No. 11, e22404, 2020.

[15] Tse, D. and P. Viswanath, *Fundamentals of Wireless Communication*, Cambridge University Press, 2005.

[16] Geyi, W., "Capacity of transmitting antenna," in *2007 IEEE Antennas and Propagation Society International Symposium*, 4052–4055, 2007.

[17] Kim, Y.-D., S.-J. Yang, Y.-S. Kang, I.-J. Hwang, and J.-W. Yu, "Mutual admittance of two arbitrary antennas in nonplanar skew positions based on infinitesimal dipole modeling," *IEEE Trans-*

actions on Antennas and Propagation, Vol. 67, No. 11, 6705–6713, Nov. 2019.

[18] Mikki, S. M. and Y. M. M. Antar, "The antenna current Green's function as an alternative method to conventional full-wave analysis solvers: An outline," in *2015 IEEE Mtt-s International Conference on Numerical Electromagnetic and Multiphysics Modeling and Optimization (NEMO)*, 1–3, 2015.

[19] Mikki, S., "The antenna spacetime system theory of wireless communications," *Proceedings of The Royal Society A*, Vol. 475, No. 2224, 20180699, Apr. 2019.

[20] Wan, Z., J. Zhu, Z. Zhang, and L. Dai, "Capacity for electromagnetic information theory," *Arxiv Preprint Arxiv:2111.00496*, 2021.

[21] Martini, A., A. Massa, and M. Franceschetti, "Physical limits to the capacity of wide-band gaussian MIMO channels," *IEEE Transactions on Wireless Communications*, Vol. 8, No. 7, 3396–3400, 2009.

[22] Yuan, S. S. A., Z. He, X. Chen, C. Huang, and W. E. I. Sha, "Electromagnetic effective degree of freedom of an MIMO system in free space," *IEEE Antennas and Wireless Propagation Letters*, Vol. 21, No. 3, 446–450, 2022.

[23] Chiurtu, N. and B. Rimoldi, "Varying the antenna locations to optimize the capacity of multi-antenna gaussian channels," in *2000 IEEE International Conference on Acoustics, Speech, and Signal Processing. Proceedings (Cat. No. 00ch37100)*, Vol. 5, 3121–3123, 2000.

[24] Sarkar, D., S. Mikki, and Y. Antar, "Fast and efficient estimation of spatial correlation characteristics of co-located dual-polarized massive MIMO arrays in 5G base stations," in *2019 Teqip III Sponsored International Conference on Microwave Integrated Circuits, Photonics and Wireless Networks (IMICPW)*, 159–162, 2019.

[25] Di Renzo, M., K. Ntontin, J. Song, F. H. Danufane, X. Qian, F. Lazarakis, J. D. Rosny, D.-T. Phan-Huy, O. Simeone, R. Zhang, *et al.*, "Reconfigurable intelligent surfaces vs. relaying: differences, similarities, and performance comparison," *IEEE Open Journal of The Communications Society*, Vol. 1, 798–807, 2020.

[26] Garcia, J. C. B., A. Sibille, and M. Kamoun, "Reconfigurable intelligent surfaces: bridging the gap between scattering and reflection," *IEEE Journal on Selected Areas in Communications*, Vol. 38, No. 11, 2538–2547, 2020.

[27] Yoo, I., M. F. Imani, T. Sleasman, H. D. Pfister, and D. R. Smith, "Enhancing capacity of spatial multiplexing systems using reconfigurable cavity-backed metasurface antennas in clustered MIMO channels," *IEEE Transactions on Communications*, Vol. 67, No. 2, 1070–1084, 2019.

[28] Liaskos, C., S. Nie, A. Tsioliaridou, A. Pitsillides, S. Ioannidis, and I. Akyildiz, "A new wireless communication paradigm through software-controlled metasurfaces," *IEEE Communications Magazine*, Vol. 56, No. 9, 162–169, 2018.

[29] Ushikoshi, D., M. Tanikawa, K. Asano, K. Sanji, M. Ikeda, D. Anzai, and H. Wakatsuchi, "Experimental demonstration of waveform-selective metasurface varying wireless communication characteristics at the same frequency band of 2.4 GHz," *Electronics Letters*, Vol. 56, No. 3, 160–162, 2020.

[30] Sarkar, D., S. Mikki, and Y. M. M. Antar, "Engineering the eigenspace structure of massive MIMO links through frequency-selective surfaces," *IEEE Antennas and Wireless Propagation Letters*, Vol. 18, No. 12, 2701–2705, 2019.

[31] Renzo, M. D., A. Zappone, M. Debbah, M.-S. Alouini, C. Yuen, J. d. Rosny, and S. Tretyakov, "Smart radio environments empowered by reconfigurable intelligent surfaces: How it works, state of research, and the road ahead," *IEEE Journal on Selected Areas in Communications*, Vol. 38, No. 11, 2450–2525, 2020.

[32] Atapattu, S., R. Fan, P. Dharmawansa, G. Wang, J. Evans, and T. A. Tsiftsis, "Reconfigurable intelligent surface assisted two–way communications: performance analysis and optimization," *IEEE Transactions on Communications*, Vol. 68, No. 10, 6552–6567, 2020.

[33] Cui, T. J., M. Q. Qi, X. Wan, J. Zhao, and Q. Cheng, "Coding metamaterials, digital metamaterials and programmable metamaterials," *Light: Science & Applications*, Vol. 3, No. 10, e218, 2014.

[34] Cui, T. J., "Microwave metamaterials," *National Science Review*, Vol. 5, No. 2, 134–136, 2018.

[35] Shuang, Y., H. Zhao, M. Wei, Q. Cheng, S. Jin, T. Cui, P. D. Hougne, and L. Li, "One-bit quantization is good for programmable coding metasurfaces," *Science China Information Sciences*, Vol. 65, No. 7, 172301, 2022.

[36] Cui, T. J., S. Liu, G. D. Bai, and Q. Ma, "Direct transmission of digital message via programmable coding metasurface," *Research*, Vol. 2019, 2019.

[37] Zhang, L., M. Z. Chen, W. Tang, J. Y. Dai, L. Miao, X. Y. Zhou, S. Jin, Q. Cheng, and T. J. Cui, "A wireless communication scheme based on space-and frequency-division multiplexing using digital metasurfaces," *Nature Electronics*, Vol. 4, No. 3, 218–227, 2021.

[38] Zhao, J., X. Yang, J. Y. Dai, Q. Cheng, X. Li, N. H. Qi, J. C. Ke, G. D. Bai, S. Liu, S. Jin, *et al.*, "Programmable time-domain digital-coding metasurface for non-linear harmonic manipulation and new wireless communication systems," *National Science Review*, Vol. 6, No. 2, 231–238, 2019.

[39] Dai, J. Y., W. K. Tang, J. Zhao, X. Li, Q. Cheng, J. C. Ke, M. Z. Chen, S. Jin, and T. J. Cui, "Wireless communications through a simplified architecture based on time-domain digital coding metasurface," *Advanced Materials Technologies*, Vol. 4, No. 7, 1900044, 2019.

[40] Dai, J. Y., W. Tang, L. X. Yang, X. Li, M. Z. Chen, J. C. Ke, Q. Cheng, S. Jin, and T. J. Cui, "Realization of multi-modulation schemes for wireless communication by time-domain digital coding metasurface," *IEEE Transactions on Antennas and Propagation*, Vol. 68, No. 3, 1618–1627, 2019.

[41] Tang, W., J. Y. Dai, M. Z. Chen, K.-K. Wong, X. Li, X. Zhao, S. Jin, Q. Cheng, and T. J. Cui, "MIMO transmission through reconfigurable intelligent surface: system design, analysis, and implementation," *IEEE Journal on Selected Areas in Communications*, Vol. 38, No. 11, 2683–2699, 2020.

[42] Tang, W., M. Z. Chen, J. Y. Dai, Y. Zeng, X. Zhao, S. Jin, Q. Cheng, and T. J. Cui, "Wireless communications with programmable metasurface: new paradigms, opportunities, and challenges on transceiver design," *IEEE Wireless Communications*, Vol. 27, No. 2, 180–187, 2020.

[43] Liaskos, C., S. Nie, A. Tsioliaridou, A. Pitsillides, S. Ioannidis, and I. Akyildiz, "A new wireless communication paradigm through software-controlled metasurfaces," *IEEE Communications Magazine*, Vol. 56, No. 9, 162–169, 2018.

[44] Cui, T.-J., S. Liu, and L.-L. Li, "Information entropy of coding metasurface," *Light: Science & Applications*, Vol. 5, No. 11, e16172, 2016.

[45] Wu, H., G. D. Bai, S. Liu, L. Li, X. Wan, Q. Cheng, and T. J. Cui, "Information theory of metasurfaces," *National Science Review*, Vol. 7, No. 3, 561–571, 2020.

[46] Wu, H., X. X. Gao, L. Zhang, G. D. Bai, Q. Cheng, L. Li, and T. J. Cui, "Harmonic information transitions of spatiotemporal metasurfaces," *Light: Science & Applications*, Vol. 9, No. 1, 198,

2020.

[47] Shao, R. W., J. W. Wu, Z. X. Wang, H. Xu, H. Q. Yang, Q. Cheng, and T. J. Cui, "Macroscopic model and statistical model to characterize electromagnetic information of digital coding metasurface," *National Science Review*, nwad299, 2023.

[48] Larsson, E. G., O. Edfors, F. Tufvesson, and T. L. Marzetta, "Massive mimo for next generation wireless systems," *IEEE Communications Magazine*, Vol. 52, No. 2, 186–195, 2014.

[49] Shlezinger, N., O. Dicker, Y. C. Eldar, I. Yoo, M. F. Imani, and D. R. Smith, "Dynamic metasurface antennas for uplink massive mimo systems," *IEEE Transactions on Communications*, Vol. 67, No. 10, 6829–6843, 2019.

[50] Dai, J. Y., W. Tang, M. Z. Chen, C. H. Chan, Q. Cheng, S. Jin, and T. J. Cui, "Wireless communication based on information metasurfaces," *IEEE Transactions on Microwave Theory and Techniques*, Vol. 69, No. 3, 1493–1510, 2021.

[51] Shannon, C. E., "A mathematical theory of communication," *Acm Sigmobile Mobile Computing and Communications Review*, Vol. 5, No. 1, 3–55, 2001.

[52] Li, H., B.-Z. Wang, L. Guo, W. Shaoand, and P. Du, "A far field pattern analysis technique for reflectarrays including mutual coupling between elements," *Journal of Electromagnetic Waves and Applications*, Vol. 23, No. 1, 87–95, 2009.

[53] Wang, K., J. Zhao, Q. Cheng, D. S. Dong, and T. J. Cui, "Broadband and broad-angle low-scattering metasurface based on hybrid optimization algorithm," *Scientific Reports*, Vol. 4, No. 1, 5935, 2014.

[54] Neder, V., Y. Ra'di, A. Alù, and A. Polman, "Combined metagratings for efficient broad-angle scattering metasurface," *ACS Photonics*, Vol. 6, No. 4, 1010–1017, 2019.

[55] Tian, T., X. Huang, Y. Xu, P. Liu, C. Liu, N. Hu, J. Zhang, and Z. Wu, "A wideband energy selective surface with quasi-elliptic bandpass response and high-power microwave shielding," *IEEE Transactions on Electromagnetic Compatibility*, 2023.

[56] Van Bladel, J. G., *Electromagnetic Fields*, John Wiley & Sons, 2007.

[57] Wan, X., M. Q. Qi, T. Y. Chen, and T. J. Cui, "Field-programmable beam reconfiguring based on digitally-controlled coding metasurface," *Scientific Reports*, Vol. 6, No. 1, 20663, 2016.

[58] Yang, H., X. Cao, F. Yang, J. Gao, S. Xu, M. Li, X. Chen, Y. Zhao, Y. Zheng, and S. Li, "A programmable metasurface with dynamic polarization, scattering and focusing control," *Scientific Reports*, Vol. 6, No. 1, 35692, 2016.

[59] Feller, W., *An Introduction to Probability Theory and Its Applications, Volume 2*, John Wiley & Sons, 1991.

[60] Kullback, S., *Information Theory and Statistics*, Courier Corporation, 1997.

[61] Blahut, R., "Computation of channel capacity and rate-distortion functions," *IEEE Transactions on Information Theory*, Vol. 18, No. 4, 460–473, 1972.

[62] Sarkar, D., S. Mikki, and Y. Antar, "An electromagnetic framework for the deployment of reconfigurable intelligent surfaces to control massive mimo channel characteristics," in *2020 14th European Conference on Antennas and Propagation (EUCAP)*, 1–4, 2020.